Hinge Spin Polarization in Magnetic Topological Insulators Revealed by Resistance Switch

Pablo M. Perez-Piskunow*
Catalan Institute of Nanoscience and Nanotechnology (ICN2), CSIC and BIST, Campus UAB, Bellaterra, 08193 Barcelona, Spain

Stephan Roche
Catalan Institute of Nanoscience and Nanotechnology (ICN2), CSIC and BIST, Campus UAB, Bellaterra, 08193 Barcelona, Spain and ICREA–Institució Catalana de Recerca i Estudis Avançats, 08010 Barcelona, Spain

(Received 28 December 2020; accepted 8 March 2021; published 20 April 2021)

We report on the possibility of detecting hinge spin polarization in magnetic topological insulators by resistance measurements. By implementing a three-dimensional model of magnetic topological insulators into a multiterminal device with ferromagnetic contacts near the top surface, local spin features of the chiral edge modes are unveiled. We find local spin polarization at the hinges that inverts the sign between the top and bottom surfaces. At the opposite edge, the topological state with inverted spin polarization propagates in the reverse direction. A large resistance switch between forward and backward propagating states is obtained, driven by the matching between the spin polarized hinges and the ferromagnetic contacts. This feature is general to the ferromagnetic, antiferromagnetic, and canted antiferromagnetic phases, and enables the design of spin-sensitive devices, with the possibility of reversing the hinge spin polarization of the currents.

DOI: 10.1103/PhysRevLett.126.167701

Introduction.—The recent discovery of intrinsic magnetic topological insulator (TI) multilayered $MnBi_2Te_4$ [1,2] has boosted the expectations for more resilient quantum anomalous Hall effect (QAHE) [3–9] and observability of axion insulator states [10–12]. The material platforms to realize the quantum anomalous Hall (QAH) phase can be classified, in a broad sense, in two- and three-dimensional systems. The former includes monolayer materials and high-symmetry models with spin-orbit coupling and magnetic exchange [13–15]. The latter is the case of three-dimensional magnetic TIs, usually realized in thin-film and few-layer systems, including magnetically doped TIs [16,17], proximitized TI surfaces with a magnetic insulator [18,19], and the Chern insulator phase of $MnBi_2Te_4$ [1,11]. The distinction that arises in three-dimensional magnetic TIs is that the topological nature comes from contributions from two Dirac-like surfaces that, upon the introduction of a magnetization field throughout the material, become massive with opposite effective masses [20,21]. Despite the three-dimensional nature of magnetic TIs, they are often analyzed near the surface as effective two-dimensional systems.

However, compared to their two-dimensional counterparts, three-dimensional magnetic TIs present a higher level of complexity that reflects in layer-to-layer magnetic exchange and termination-dependent surface states, which ultimately dictate the nature and properties of surface magnetism and of topological edge states [22–24]. The spin texture of topological edge states in both the quantum spin Hall and QAH regimes is usually perpendicular to the material's surface, limiting the possibility for magnetic-sensitive detection or further spin manipulation protocols [25]. The effective two-dimensional models of these materials are often highly symmetric and may overlook the sublattice and spin degree of freedom. However, spin textures [26], spin Hall conductivity [27], and local spin polarization [28] provide great insight into the special topological phases that can arise in topological superconductors and boundary-obstructed TIs [29,30]. By reducing the symmetry constraints, new spin textures can develop, such as hidden spin polarization [31] and canted spin textures [32–34]. In the presence of a uniform [35] or alternating [36] Zeeman field, several models of magnetic layers exhibit high-order topological phases and cleavage-dependent hinge modes [35–41]. Thus, a detailed study of the spin features on a spinful three-dimensional model of the QAHE realized in magnetic TI multilayers is missing.

In this Letter, we use the generic Fu-Kane-Mele (FKM) model for three-dimensional topological insulators [42] and introduce exchange terms to describe both ferromagnetic (FM) and antiferromagnetic (AFM) multilayered TIs. Contrary to ordinary spin-z polarization of edge states in the QAH regime, the model exhibits an in-plane *hinge spin polarization* (HSP) which becomes apparent (and

observable) in a specific device setup. Indeed, the topological states are characterized by an in-plane HSP perpendicular to both the current flow and the sample magnetization direction. The in-plane polarization reverses sign along the vertical direction between the top and bottom surfaces. By using efficient quantum transport simulation methods [43] implemented into a three-dimensional multiterminal device, such peculiar local spin polarization is shown to give rise to a giant resistance switching (or *spin valve*) triggered upon either inverting the magnetization of the sample, varying the polarization of the magnetic detectors, or reversing the current direction. The appearance of HSP in the QAH regime is rooted in the chiral-like [26,40] symmetries of the lattice and on the half-quantization of the topological charge at the surfaces [21,44–47]. Therefore, the HSP fingerprints are highly robust to Anderson energetic disorder, and to structural edge disorder.

Hamiltonian of the three-dimensional magnetic TI.— The magnetic TI is described by a three-dimensional (diamond cubic lattice) FKM Hamiltonian [42,48,49], with magnetic layers modeled by an exchange coupling term that well captures the effect of magnetic impurities [50] or magnetic layers [35,51]. To simulate a multilayer FM or AFM magnetic TI, we tune the orientation of the magnetic moments per layer. The FKM lattice vectors are $\boldsymbol{a}_1 = (1/2, -\sqrt{1/3}/2, \sqrt{2/3})$, $\boldsymbol{a}_2 = (0, \sqrt{1/3}, \sqrt{2/3})$, and $\boldsymbol{a}_3 = (-1/2, -\sqrt{1/3}/2, \sqrt{2/3})$; each unit cell has two sublattices: A with $\mathbf{0}$ offset, and B with offset $\boldsymbol{d}_4 = (0, 0, \sqrt{3/2}/2)$. The other first neighbors of A sites are at relative positions $\boldsymbol{d}_q = \boldsymbol{d}_4 - \boldsymbol{a}_q$ for $q = 1, 2, 3$. The full Hamiltonian reads

$$\mathcal{H}_0 = \sum_{\langle i,j\rangle}\sum_{\alpha} c^{\dagger}_{i,\alpha} t_{ij} c_{j,\alpha}; \qquad \mathcal{H}_Z = \sum_{i,\alpha,\beta} c^{\dagger}_{i,\alpha} [\boldsymbol{m}_i \cdot \boldsymbol{s}]_{\alpha,\beta} c_{i,\beta}$$

$$\mathcal{H}_{\mathrm{SO}} = i\frac{8\lambda_{\mathrm{SO}}}{a^2}\sum_{\langle\langle i,j\rangle\rangle}\sum_{\alpha,\beta} c^{\dagger}_{i,\alpha}[\boldsymbol{s}\cdot(\boldsymbol{d}^1_{ij}\times\boldsymbol{d}^2_{ij})]_{\alpha,\beta} c_{j,\beta}$$

$$\mathcal{H} = \mathcal{H}_0 + \mathcal{H}_{\mathrm{SO}} + \mathcal{H}_Z, \tag{1}$$

with latin indices for lattice sites, and Greek indices for spin value in the s_z basis. The Zeeman magnetization vector $\boldsymbol{m}_i$ may depend on the layer of the orbital i, and $\boldsymbol{s}$ is a vector of Pauli matrices acting on the spin degree of freedom. The parameter λ_{SO} denotes the spin-orbit (SO) coupling strength, while t_{ij} describes the nearest neighbors coupling between sites i and j, and takes different values t_q with $q = 1, \ldots, 4$ depending on the direction $\boldsymbol{r}_j - \boldsymbol{r}_i = \boldsymbol{d}_q$. As described in Fu *et al.* [42], the isotropic case $t_q = t$ defines a multicritical point. Adding anisotropy $t_q = t$ for $q = 1, 2, 3$ and $t_4 > t$, sets the phase to a strong TI characterized by a nontrivial $\mathcal{Z}_2$ invariant. We tune the parameters to the strong TI phase with $t_4 = 1.4t$ and $\lambda_{\mathrm{SO}} = 0.1t$ [52]. The FKM model can be interpreted as a stack of coupled Rashba layers, with an alternating Rashba field [36,53]. In absence of a Zeeman field, the strong TI phase is the three-dimensional realization of the Shockley model [53], hosting sublattice polarized surface states. The magnetic moments per layer describe the AFM (alternating magnetization between layers $\boldsymbol{m}_i = \pm\boldsymbol{m}$) or FM (constant magnetization $\boldsymbol{m}_i = \boldsymbol{m}$) coupling between layers. In a slab geometry perpendicular to the z axis, a Zeeman exchange coupling field $\boldsymbol{m} = 0.05t\hat{z}$ opens a gap on the surface states and sets the QAH phase described by a nontrivial Chern number [54].

We present the main electronic and spin characteristics of the magnetic topological insulator model in Fig. 1. The details of the edge modes vary with the geometric design. For a heterostructure infinite along the y direction but finite in both other directions, we obtain the usual linear energy dispersion of topological edge states seen in Fig. 1(a). These states cover the whole side surface of the stack (wall

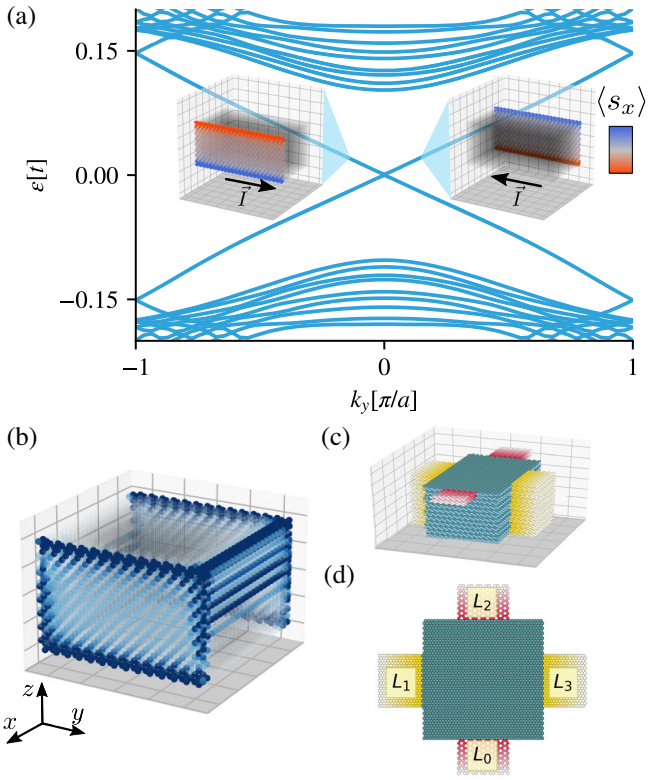

FIG. 1. Magnetic TI in the FM phase, $\boldsymbol{m} = 0.05t\hat{z}$. (a) Dispersion relation of a slab geometry infinite in the y direction. The left (right) inset depicts the local spin density of states $\langle s_x \rangle$ of the edge state at $k_y = -0.1\pi/a$ ($k_y = 0.1\pi/a$). The edge state covers the sidewall of the slab and propagates to the right (left). (b) Local density of states of a finite square slab. The edge state circulates around the sample, covers the side surfaces perpendicular to $\hat{x}$, and propagates along the top or bottom hinges of the side surfaces perpendicular to $\hat{y}$. (c) Side view of transport setup geometry: metallic leads connect to the whole walls at both ends of the slab (golden color), and ferromagnetic leads connect to the sidewalls only near top hinge (red color). (d) Top view and reference numbering of the leads on the transport setup.

states) with a very large electronic density at the hinges. Interestingly, the projected local spin density of the wall states is seen to be dominated by the $\langle s_x \rangle$ value near the hinges. The HSP switches sign between opposite surfaces. Furthermore, the HSP changes sign for the back-propagating states, located at the opposite walls (see insets). On a finite slab, Fig. 1(b), the nature of the chiral states becomes richer, with the emergence of hinge states for certain surface cleavage orientations, a property predicted for *Möbius* fermions [35,36,40]. The Möbius fermion phase depends on the ferromagnetic interlayer exchange and appears in the FM and canted AFM phase on crystalline canting directions. Conversely, the HSP is robust and appears in all phases, that is, FM, AFM, and canted AFM, irrespective of the canting angle, as long as there is a z component of the net magnetization. Next, we explore the possible fingerprints of such anomalous spin features on quantum transport in the QAH regime.

Multiterminal spin transport simulations.—To analyze the spin transport in the QAH regime, we use the Kwant software package [43] to build the three-dimensional model and implement a multiterminal device configuration, shown in Figs. 1(c) and 1(d). We perform charge transport simulations of a central scattering region connected with metallic and ferromagnetic leads. The interplay between the states available for transport in the leads and in the scattering region has a central role. The leads L_1 and L_3 are the metallic leads (golden color). They are fully contacting the left and right sides of the slab (all spin projections). The ferromagnetic leads L_0 and L_2 (red color) located on the sides only contact the upper part of the device near the top hinge [55]. They carry electrons with only one spin polarization: $(s_x, \downarrow)$. In this way, these contacts couple with the edge state in the region of maximal local spin polarization.

The expected resistance measurements for the QAHE are shown in the inset of Fig. 2. We use the notation $R_{ij,kl}$, for the resistance measured from passing current between terminals i and j and measuring the voltage drop between terminals k and l. The two-terminal (2T) resistance $R_{kl,kl}$ is noted $R_{2T,kl}$. The typical values of Hall resistance $R_{xy} = R_{13,20}$ and the longitudinal resistance $R_{xx} = R_{01,23}$ of a QAH insulator [56,57] take the quantized values $R_{xy} = (1/C)h/e^2$, where C is the Chern number, and vanishing R_{xx} inside the gap. The two-terminal resistance $R_{2T} = h/e^2$ is also quantized for perfect tunneling between the leads and the scattering region [58]. Such is the case of the matching ferromagnetic lead. The matching or mismatching between the spin current carried by the leads and the spin polarization of the edge states gives rise to a remarkable resistance switch, as seen in Fig. 2. The 2T resistance in the matching case is quantized inside the topological gap, while in the mismatching case the resistance increases by more than 1 order of magnitude.

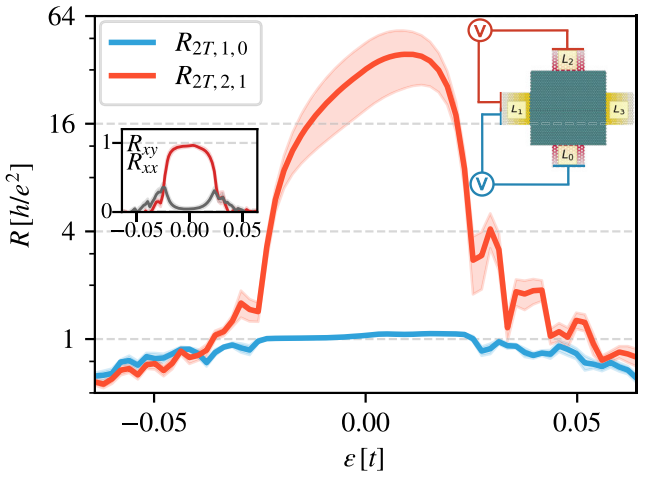

FIG. 2. Transport simulations of a FM slab ($\boldsymbol{m} = 0.02t\hat{z}$) between metallic leads and ferromagnetic leads with spin down $(s_x, \downarrow)$ polarization. The shaded regions depict the standard error of considering ten Anderson disorder realizations of strength $d = 0.04t$. A four-terminal device allows us to measure the distinct resistance profiles. The two-terminal resistance setup between leads L_0 and L_1 is depicted in the left inset and the blue curve is the resistance profile. The right inset shows the resistance setup between leads L_1 and L_2, with resistance profile in red. In the former case, the ferromagnetic lead polarization matches the top HSP, and in the latter case, the local spin polarization is opposite.

To test the robustness of the 2T resistance switching effect, we introduce different types of disorder. First, we consider the impact of structural disorder—vacancies near the sidewalls of the slab. This disorder is detrimental to the formation of well-defined HSP, which only occurs for wall states at crystalline edges. Nevertheless, it is relevant for predictions on experiments, since the side walls of material samples have edge disorder. We find that the HSP effect survives to structural disorder, up to %5 vacancies [52]. Next, we simulate Anderson disorder by adding an on-site energy $d\chi$, where χ is a random variable with normal distribution on $[-0.5, 0.5)$. We find robustness of the HSP up to d much larger than the magnetization strength. In Fig. 2, we use $d = 2|\boldsymbol{m}| = 0.04t$, and average the resistance curve over ten disorder realizations. We see that spin transport measurements can still distinguish the peculiar spin texture of the edge states.

The fact that Anderson disorder and structural disorder show the resistance switch is crucial in establishing the robustness of our results. The limit mismatching case, where the edge state and ferromagnetic lead are completely decoupled from the transport setup, results in voltage probes that have zero transmission probability to any other leads, leaving a floating probe with an arbitrary value of the chemical potential and the voltage [59]. However, in our case, the ferromagnetic leads are not fully disconnected when the spins do not match, rather they are weakly connected. Even though the value of the 2T resistance is

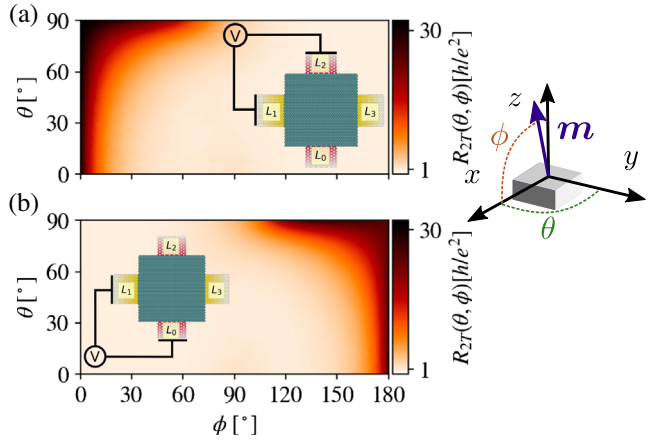

FIG. 3. 2T resistance at $e_F = 0$ of a magnetic TI slab in the FM phase, with magnetization $|\boldsymbol{m}| = 0.02t$ (see right inset). In (a), the two-terminal resistance is measured between leads L_1 and L_2; in (b), the resistance is measured between leads L_0 and L_1. The plots in (a) and (b) are almost identical by reflecting around $\phi = 90°$, where the magnetization component along the z axis changes sign. The mismatching configurations $\phi = 0°$ in (a), and $\phi = 180°$ in (b) show the largest resistance that slowly decreases when rotating the magnetization angle.

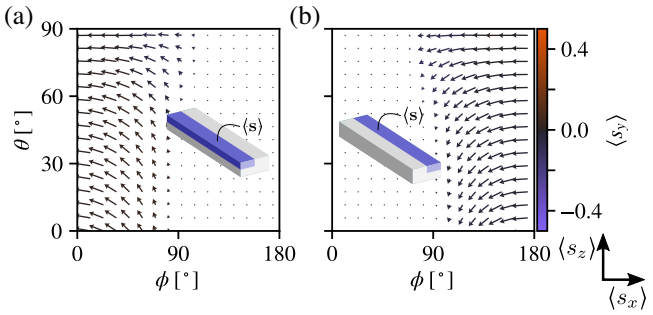

FIG. 4. Magnetic TI slab with the same parameters as in Fig. 3. HSP of the edge state at $k_y = -0.02\pi/a$ and positive energy (propagating in the $\hat{y}$ direction) for a wide range of magnetization angles (θ, ϕ). The arrows show the components of $\langle s \rangle$ projected on the top-left (-right) hinges of an infinite slab along the y axis. The direction of the arrows gives the component in the $(\langle s_x \rangle, \langle s_z \rangle)$ plane, and the color of the arrows is the component in $\langle s_y \rangle$. (a) Propagating edge states on the top-left hinge are only present when the magnetization has a positive projection along z, thus, $\phi \lesssim 90°$. (b) Propagating edge states on the top-right hinge are only present when the magnetization has a negative projection along z, thus, $\phi \gtrsim 90°$.

sensitive to the details of the weak coupling, seen on the large standard error in Fig. 2, the trend is clear. In a QAH thin film contacted on its lateral sides with ferromagnetic leads, we can selectively get either full transmission or blocking of the edge state transport. Such a phenomenon is sensitive to the direction of the magnetization of the ferromagnetic leads, the direction of the current, and the net magnetization of the sample.

Another experimentally relevant analysis is to explore the resistance switch for different directions of the magnetization $\boldsymbol{m}$ of the slab in the FM phase. Figure 3 shows two measures of 2T resistance, as in Fig. 2 at the charge neutrality point, for different directions of the Zeeman exchange field $(\cos\theta\cos\phi\hat{x} + \sin\theta\cos\phi\hat{y} + \sin\phi\hat{z})$ (see right inset). At low ϕ angles ($\boldsymbol{m}$ pointing mostly toward $+\hat{z}$), the configuration $R_{2T,1,2}$ in 3(a) shows large resistance, while $R_{2T,0,1}$ in 3(b) is close to the quantized value h/e^2. When sweeping the magnetization to the inverse direction (toward $-\hat{z}$) at $\phi 180°$, the roles of 3(a) and 3(b) reverse, giving a clear signature of the highly spin-polarized hinges and of the spin-dependent matching and mismatching with the ferromagnetic leads. In the middle of both extremes, where $\phi = 90°$, the magnetization lies in the plane of the slab and does not open a gap on the top and bottom surfaces. At intermediate angles, we note that the resistance switch is more robust for $\theta = 90°$, where $\boldsymbol{m}$ tilts toward $\hat{y}$, the transport direction and edge direction that the FM leads contact.

The HSP of the edge states is a good proxy for predicting the switch in resistances that is measured in the device shown in Fig. 3. We obtain the spin projection of the forward propagating edge states on the top half of an infinite slab in the $\hat{y}$ direction, and finite in the xz plane, see insets of Fig. 4. At momentum $k = -0.02\pi/a$ we select the positive eigenvalue inside the topological gap, similar to the states shown in the insets of Fig. 1(a). Panels (a) and (b) of Fig. 4 show finite length arrows that indicate the spin density and components in the $(\langle s_x \rangle, \langle s_z \rangle)$ plane of the forward propagating state, while the color represents the mostly null $\langle s_y \rangle$ component. A vanishing arrow length (a point in the plot) indicates that there is no net spin density at that region enclosing that hinge [60]. When the system is in the topological phase ($\phi \sim 90°$), there is electronic density in one edge or the other, and spin density near the hinge (a finite arrow). Accordingly, we see that panel 4(b) complements perfectly panel 4(a). In both cases, the HSP direction changes with the magnetization angle, giving a notch to control the matching or mismatching cases in a transport setup.

Conclusions.—We have demonstrated that the edge states in thin-film ferromagnetic and antiferromagnetic TIs host HSP, spin polarized states at the hinges, which leads to a large resistance switch. The HSP of the edge states is in plane, but the sign depends on the propagation direction and the magnetization of the sample. For a crystalline edge direction, the local spin polarization reverses across the vertical direction. Thus, the HSP inverts across the vertical direction, and switches sign for the opposite current direction. Carefully engineering ferromagnetic contact leads in a transport setup allows us to obtain a *giant resistance* (*spin valve effect*) upon reversing the current direction or, conversely, tuning the total magnetization of the sample. The $\langle s_x \rangle$ component of the

spin direction in Figs. 4(a) and 4(b) can be directly translated to the resistance values found in Figs. 3(a) and 3(b). This highlights that the resistance switching mechanism, once established, can be used to gain insight about the magnetization of the sample.

Finally, we observe the fact that FM and AFM topological insulators are able to host maximally spin polarized currents along crystalline hinges opens new avenues to implement disruptive proposals using axion and magnetic TIs to manipulate dislocation, hinge, and edge states [37], with the additional value of spin polarization features.

We thank Sergio O. Valenzuela, David Soriano, and Aron W. Cummings for fruitful discussions. We acknowledge the European Union Horizon 2020 research and innovation programme under Grant Agreement No. 824140 (TOCHA, H2020-FETPROACT-01-2018). ICN2 is funded by the CERCA Programme/Generalitat de Catalunya, and is supported by the Severo Ochoa program from Spanish MINECO (Grant No. SEV-2017-0706).

*pablo.perez.piskunow@gmail.com

[1] M. M. Otrokov *et al.*, Nature (London) **576**, 416 (2019).
[2] I. I. Klimovskikh *et al.*, npj Quantum Mater. **5**, 54 (2020).
[3] F. D. M. Haldane, Phys. Rev. Lett. **61**, 2015 (1988).
[4] C. Z. Chang *et al.*, Science **340**, 167 (2013).
[5] Y. Deng, Y. Yu, M. Z. Shi, Z. Guo, Z. Xu, J. Wang, X. H. Chen, and Y. Zhang, Science **367**, 895 (2020).
[6] T. Hirahara *et al.*, Nat. Commun. **11**, 4821 (2020).
[7] D. A. Estyunin, I. I. Klimovskikh, A. M. Shikin, E. F. Schwier, M. M. Otrokov, A. Kimura, S. Kumar, S. O. Filnov, Z. S. Aliev, M. B. Babanly, and E. V. Chulkov, APL Mater. **8**, 021105 (2020).
[8] S. Wimmer *et al.*, arXiv:2011.07052.
[9] V. Bonbien, F. Zhuo, A. Salimath, O. Ly, A. Abbout, and A. Manchon, arXiv:2102.01632.
[10] D. Zhang, M. Shi, T. Zhu, D. Xing, H. Zhang, and J. Wang, Phys. Rev. Lett. **122**, 206401 (2019).
[11] C. Liu, Y. Wang, H. Li, Y. Wu, Y. Li, J. Li, K. He, Y. Xu, J. Zhang, and Y. Wang, Nat. Mater. **19**, 522 (2020).
[12] F. Giustino *et al.*, J. Phys. Mater. **3**, 042006 (2021).
[13] Z. Qiao, S. A. Yang, W. Feng, W.-K. Tse, J. Ding, Y. Yao, J. Wang, and Q. Niu, Phys. Rev. B **82**, 161414(R) (2010).
[14] W.-K. Tse, Z. Qiao, Y. Yao, A. H. MacDonald, and Q. Niu, Phys. Rev. B **83**, 155447 (2011).
[15] An alternative route to realize the QAHE is to include strong interactions, leading to orbital magnetization, see F. Zhang, J. Jung, G. A. Fiete, Q. Niu, and A. H. MacDonald, Phys. Rev. Lett. **106**, 156801 (2011); W. Chen and J. L. Lado, Phys. Rev. Lett. **122**, 016803 (2019); M. Serlin, C. L. Tschirhart, H. Polshyn, Y. Zhang, J. Zhu, K. Watanabe, T. Taniguchi, L. Balents, and A. F. Young, Science **367**, 900 (2020).
[16] G. Xu, J. Wang, C. Felser, X.-L. Qi, and S.-C. Zhang, Nano Lett. **15**, 2019 (2015).
[17] S. Qi, Z. Qiao, X. Deng, E. D. Cubuk, H. Chen, W. Zhu, E. Kaxiras, S. B. Zhang, X. Xu, and Z. Zhang, Phys. Rev. Lett. **117**, 056804 (2016).
[18] Y. Hou, J. Kim, and R. Wu, Sci. Adv. **5**, eaaw1874 (2019).
[19] M. Mogi, T. Nakajima, V. Ukleev, A. Tsukazaki, R. Yoshimi, M. Kawamura, K. S. Takahashi, T. Hanashima, K. Kakurai, T.-h. Arima, M. Kawasaki, and Y. Tokura, Phys. Rev. Lett. **123**, 016804 (2019).
[20] R. Yu, W. Zhang, H.-J. Zhang, S.-C. Zhang, X. Dai, and Z. Fang, Science **329**, 61 (2010).
[21] R.-L. Chu, J. Shi, and S.-Q. Shen, Phys. Rev. B **84**, 085312 (2011).
[22] Y. Tokura, K. Yasuda, and A. Tsukazaki, Nat. Rev. Phys. **1**, 126 (2019).
[23] X. Wu *et al.*, Phys. Rev. X **10**, 031013 (2020).
[24] D. Nevola, H. X. Li, J.-Q. Yan, R. G. Moore, H.-N. Lee, H. Miao, and P. D. Johnson, Phys. Rev. Lett. **125**, 117205 (2020).
[25] For tunable spin polarization in the QAHE see R.-X. Zhang, H.-C. Hsu, and C.-X. Liu, Phys. Rev. B **93**, 235315 (2016).
[26] A 2D model including sublattice and spin can yield in-plane spin polarization, see J. Wu, J. Liu, and X.-J. Liu, Phys. Rev. Lett. **113**, 136403 (2014).
[27] M. Costa, G. R. Schleder, C. M. Acosta, A. C. M. Padilha, F. Cerasoli, M. B. Nardelli, and A. Fazzio, arXiv:2006.07270.
[28] K. Plekhanov, N. Müller, Y. Volpez, D. M. Kennes, H. Schoeller, D. Loss, and J. Klinovaja, Phys. Rev. B **103**, L041401 (2021).
[29] A study of the quantum spin Hall effect in magnetic topological insulators indicates the presence of hinged quantum spin Hall states, characterized by a nontrivial spin-Chern number, see Y.-r. Ding, D.-h. Xu, C.-z. Chen, and X. C. Xie, Phys. Rev. B **101**, 041404(R) (2020); However similar, our model cannot be characterized by the spin-Chern number due to the large SO coupling and nonconservation of the spin, see E. Prodan, Phys. Rev. B **80**, 125327 (2009); and D. Monaco and L. Ulčakar, Phys. Rev. B **102**, 125138 (2020). Instead, our model is characterized by a nonzero Chern number.
[30] E. Khalaf, W. A. Benalcazar, T. L. Hughes, and R. Queiroz, arXiv:1908.00011, [Phys. Rev. X, (to be published)].
[31] X. Zhang, Q. Liu, J.-W. Luo, A. J. Freeman, and A. Zunger, Nat. Phys. **10**, 387 (2014).
[32] L.-k. Shi and J. C. W. Song, Phys. Rev. B **99**, 035403 (2019).
[33] M. Vila, C.-H. Hsu, J. H. Garcia, L. A. Benítez, X. Waintal, S. Valenzuela, V. M. Pereira, and S. Roche, arXiv:2007.02053.
[34] J. H. Garcia, M. Vila, C.-H. Hsu, X. Waintal, V. M. Pereira, and S. Roche, Phys. Rev. Lett. **125**, 256603 (2020).
[35] F. Zhang, C. L. Kane, and E. J. Mele, Phys. Rev. Lett. **110**, 046404 (2013).
[36] K. Plekhanov, F. Ronetti, D. Loss, and J. Klinovaja, Phys. Rev. Research **2**, 013083 (2020).
[37] N. Varnava and D. Vanderbilt, Phys. Rev. B **98**, 245117 (2018).
[38] L. Trifunovic and P. W. Brouwer, Phys. Status Solidi (b) **258**, 2000090 (2021).
[39] Y. Tanaka, R. Takahashi, T. Zhang, and S. Murakami, Phys. Rev. Research **2**, 043274 (2020).

[40] R.-X. Zhang, F. Wu, and S. Das Sarma, Phys. Rev. Lett. **124**, 136407 (2020).
[41] For a similar model describing magnons, see A. Mook, S. A. Díaz, J. Klinovaja, and D. Loss, arXiv:2010.04142.
[42] L. Fu, C. L. Kane, and E. J. Mele, Phys. Rev. Lett. **98**, 106803 (2007).
[43] C. W. Groth, M. Wimmer, A. R. Akhmerov, and X. Waintal, New J. Phys. **16**, 063065 (2014).
[44] X.-L. Qi, T. L. Hughes, and S.-C. Zhang, Phys. Rev. B **78**, 195424 (2008).
[45] M. Gu, J. Li, H. Sun, Y. Zhao, C. Liu, J. Liu, H. Lu, and Q. Liu, arXiv:2005.13943.
[46] R. Lu *et al.*, Phys. Rev. X **11**, 011039 (2021).
[47] We verified the half-quantized topological charge at the surfaces using the method described in D. Varjas, M. Fruchart, A. R. Akhmerov, and P. M. Perez-Piskunow, Phys. Rev. Research **2**, 013229 (2020).
[48] L. Fu and C. L. Kane, Phys. Rev. B **76**, 045302 (2007).
[49] D. Soriano, F. Ortmann, and S. Roche, Phys. Rev. Lett. **109**, 266805 (2012).
[50] Q. Liu, C.-X. Liu, C. Xu, X.-L. Qi, and S.-C. Zhang, Phys. Rev. Lett. **102**, 156603 (2009).
[51] J. Wang, B. Lian, H. Zhang, and S.-C. Zhang, Phys. Rev. Lett. **111**, 086803 (2013).
[52] See the Supplemental Material at http://link.aps.org/supplemental/10.1103/PhysRevLett.126.167701 for more details on the model and structural disorder simulations.
[53] S. S. Pershoguba and V. M. Yakovenko, Phys. Rev. B **86**, 075304 (2012).
[54] C.-X. Liu, S.-C. Zhang, and X.-L. Qi, Annu. Rev. Condens. Matter Phys. **7**, 301 (2016).
[55] A similar device can be envisioned to measure the axion insulator phase R. Chen, S. Li, H.-P. Sun, H.-Z. Lu, and X. C. Xie, arXiv:2005.14074.
[56] M. Büttiker, Phys. Rev. B **38**, 9375 (1988).
[57] M. Büttiker, Phys. Rev. Lett. **57**, 1761 (1986).
[58] In the case of all normal (metallic) leads, we obtain the typical quantized values of $R_{xx} = 0$, $R_{xy} = h/e^2$, and $R_{2T,ij} = h/e^2$ for all pairs of leads i, j. This is due to the fact that metallic leads carry current with any spin projection, thus, metallic leads always realize the matching case.
[59] In the Ladauer-Bttiker formalism, after setting one reference probe L_0 with an arbitrary voltage value V_0, we eliminate the rows and columns of L_0 from the transmission matrix to make it nonsingular. However, if there is a disconnected voltage probe L_d, there is one extra row and column with zero values corresponding to L_d, and this matrix is again singular. The value that the voltage can take in this probe V_d is arbitrary, and we must eliminate the corresponding column and row to solve the system.
[60] The norm of the spin components is not conserved, since it can be averaged out within the region where it is computed. Therefore, the arrows may vanish without a significant $\langle s_y \rangle$ component.